Laser annealing for radiatively broadened MoSe_{2} grown by chemical vapor deposition

Christopher Rogers, Dodd Gray, Nate Bogdanowicz, and Hideo Mabuchi

Phys. Rev. Materials **2**, 094003 — Published 17 September 2018

DOI: 10.1103/PhysRevMaterials.2.094003

Laser Annealing for Radiatively Broadened $MoSe_2$ grown by Chemical Vapor Deposition

Christopher Rogers,* Dodd Gray, Nate Bogdanowicz, and Hideo Mabuchi†
Ginzton Laboratory, Stanford University, 348 Via Pueblo, Stanford, CA 94305
(Dated: August 29, 2018)

We report on a laser annealing procedure which greatly improves the quality of suspended monolayers of chemical vapor deposition (CVD) grown $MoSe_2$. Annealing with a green laser locally heats the suspended flake to approximately 600 K, which both removes contaminants and reduces strain gradients. At 4 K, we observe linewidths as narrow as 3.5 meV (1.6nm) full-width at half-max (FWHM) for both photoluminescence (PL) and reflection. Large peak reflectances up to 47% are also observed. These values are comparable to those of the highest quality hexagonal boron nitride (hBN) encapsulated samples. We demonstrate that this laser annealing process can yield highly spatially homogeneous samples, with the length scale of the homogeneity limited primarily by the size of the suspended area. Annealed regions are very stable, exhibiting negligible deterioration over 24 hours at cryogenic temperatures. The annealing method is also very repeatable, with substantial improvements of sample quality on every spot (> 40) tested.

I. INTRODUCTION

Recently, there has been tremendous interest in layered transition metal dichalcogenides (TMDCs). This was sparked by the discovery that the canonical TMDC MoS_2 becomes a direct bandgap semiconductor when isolated in monolayer form [1, 2]. Many of the TMDCs have since been shown to exhibit a strong excitonic feature, showing strong and spectrally narrow PL and reflection. Since then, many other TMDCs have been isolated in monolayer form, exhibiting interesting coherence [3], spin-valley [4, 5], non-linear optical [6, 7] and strain [8] properties. TMDCs have become a popular testbed for many-body electron physics [9, 10] and have attracted attention in the quantum optics community due to their potential applicability to exotic exciton-polariton condensates and quantum dot arrays deterministically patterned with electrostatic gating [11] or engineered strain [12].

Mechanical exfoliation [1, 2, 13] is one of the most popular methods to produce monolayer flakes, and while it is possible to produce very high quality flakes in this manner, the samples tend to be small ($\sim$10 µm for TMDCs). Flakes produced by mechanical exfoliation are also typically somewhat n-doped, so that electrostatic control is necessary to make the semiconductor neutral [10, 14].

The highest quality flakes are produced by mechanical exfoliation and subsequent encapsulation in hBN [15–17]. Typically, encapsulation leads to even smaller flake sizes and is a time-consuming process. These samples are often annealed in air or inert gas either during or after heterostructure fabrication to reduce contaminants between layers [15]. Microscopic spatial inhomogeneity of the exciton resonance energy is ubiquitous in exfoliated and encapsulated TMDC samples. Even the highest quality samples demonstrated to date (as measured by linewidth and peak reflectance) exhibit uncontrolled linewidth-scale spatial variation of the exciton resonance over < 3 µm [16], and 10 meV variation over ~ 15 µm [15]. This severely limits the rate of scientific progress in understanding TMDC exciton physics and presents a barrier that must be overcome for practical scaling of TMDC-based optical and electronic devices. The inhomogeneity is due to a combination of strain gradients[18], material defects [19, 20], electrostatic substrate doping effects [21] and surface contamination.

Monolayers can also be directly grown on substrates, typically by CVD. This leads to much larger flakes, up to 100 µm single crystal and continuous wafer-scale polycrystalline [22, 23]. While many interesting effects and devices have been demonstrated using CVD grown TMDCs, these monolayers are much lower quality [24] by at least several important metrics (most notably PL and reflection linewidth at low temperature) when compared to mechanically exfoliated flakes. This is despite the fact that defect densities in CVD and exfoliated monolayers are comparable [19]. The lower quality of CVD monolayers is likely due to a combination of adsorbed contaminants that are difficult to remove, and strain gradients from the growth/transfer processes [25, 26].

We report on a laser annealing procedure for improving the quality of monolayers of the TMDC $MoSe_2$ to levels comparable with hBN-encapsulated samples. The process can be tuned to yield highly spatially homogeneous samples. It is also repeatable, in the sense that annealing significantly improved sample quality on every spot tested. The annealing process involves heating suspended monolayers of $MoSe_2$ to between 500 and 600 K in high vacuum using an above-bandgap green laser. Note that this is done in a cryostat, so that the nominal substrate temperature is 4 K. Unless otherwise mentioned, all measurements were performed at 4 K and $2 \cdot 10^{-7}$ Torr. We hypothesize that this heating effectively removes contaminants and extrinsic dopants adsorbed on the monolayer. The heating in a radially symmetric manner also relaxes the strain pinning at the edge of the suspended layer and

* cmrogers@stanford.edu
† hmabuchi@stanford.edu

the spatial strain gradient is dramatically reduced. A schematic of the annealing process is shown in Fig. 1a.

II. NARROW PL AND REFLECTION IN LASER ANNEALED $MoSe_2$

Figs. 1c,1d show some of the narrowest PL and reflection from the annealed monolayers. The PL reflection full-width at half-max (FWHM) are both 3.5 meV. This is comparable to the range of 2.4-4.9 meV, for PL from high quality encapsulated $MoSe_2$ samples from [15]. It is worth noting that the dielectric environment for our suspended samples is much different than that for encapsulated samples. Excitons in encapsulated $MoSe_2$ see a larger effective dielectric constant and thus have a smaller binding energy [27]. This higher effective dielectric constant in turn leads to a longer radiative lifetime and smaller exciton radius [28]. Thus, the intrinsic radiative lifetime in suspended layers is smaller than that for encapsulated layers. Therefore, even in a system free of defects, contaminants and strain, at zero temperature (where the exciton is purely radiatively broadened), the linewidth of encapsulated samples would be smaller than that of suspended samples.

Typical PL and reflection spectra both before and after annealing are shown in Fig 1e. After annealing, the PL shows a drastic reduction in linewidth. The trion PL X^- is also reduced to negligible intensity, indicating that the annealed sample is neutral. We attribute these effects primarily to removal of contaminants from the surface of the sample. It has been shown that water and oxygen are among the primary adsorbents that can cause PL modulation through charge transfer [29], and thus it seems likely that the annealing process reduces doping by removing these and other adsorbed molecules. The disappearance of X^- emission after annealing is strong evidence that there is no intrinsic photodoping effect in $MoSe_2$. Adsorbed molecules could lead to atomic-scale variations in the dielectric and electrostatic environment seen by the exciton, manifesting as inhomogeneous broadening of the X^0 and X^- frequency. The intensity of the X^D emission (often associated with defect emission [29]) is also reduced below the noise floor of our measurements. This suggests that X^D is also due to the interaction of excitons with molecules adsorbed on the $MoSe_2$ monolayer.

The spectrum with the highest peak reflection of from an annealed spot is shown in 1g. Assuming a simple Lorentzian model for the reflection including dephasing, radiative decay, and non-radiative decay terms, a peak reflection of 47% indicates that the exciton is radiatively broadened. The maximum reflection $R_{\max}$ of the exciton feature is related to the radiative broadening Γ and the total linewidth broadening γ_{tot} by $R_{\max} = \frac{\Gamma^2}{\gamma_{\text{tot}}^2}$ [16, 17]. This leads to a ratio between radiative and all other broadening of $\frac{\Gamma}{\gamma_{\text{tot}}-\Gamma} = \frac{\sqrt{R_{\max}}}{1-\sqrt{R_{\max}}}$. The maximum reflection of 47% observed here thus corresponds to a ratio of 2.2 between radiative broadening and all other broadening and a radiative broadening of 4.3 meV.

Here we note that after annealing the sample properties were very stable. There were no appreciable changes over 24 hours (the longest time over which we measured), when the samples were kept at high vacuum ($2{\cdot}10^{-7}$) and the cryostat was kept at its base temperature of 4 K. An example of the reflection immediately after annealing and 24 hours after annealing is shown in Fig 1h. The reflection changes very little over 24 hours. The small changes that are present may be due to the fact that there is some unavoidable drift in the system, which leads to change in both the coupling efficiency of the collection and the location of the spot on the sample. We expect that the samples would also be stable under high vacuum at room temperature, although we were not able to test this in our system, which relies on cryo-pumping to achieve high vacuum. The flake quality degrades somewhat after warming and leaving at room temperature and 1 Torr for 24 hours, and then cooling back down. For the data in Fig. S2 from the SI (Supporting Information) [30], the PL linewidth went from 5.6 meV after annealing to 7.0 meV after the warm-up cycle. Note that since the holes in the substrate are closed, any contaminants removed from the bottom of the suspended film by the annealing are trapped, and may re-adsorb when the entire sample is heated to room temperature. However, these degraded flakes are higher quality than before annealing, and the degradation can be fully reversed by re-annealing. In the case of Fig. S2 from the SI [30], the linewidth is improved to 5.3 meV after re-annealing.

III. HIGH SPATIAL HOMOGENEITY IN LASER ANNEALED $MoSe_2$

It is possible to improve the spatial homogeneity of the annealed samples by raster scanning the annealing laser over the entire suspended area. This more fully removes contaminants from the entire suspended area, and can also have implications for the spatial strain gradient present in the flake. PL after annealing in the center with a laser spot much smaller than the hole (no raster scan) is shown in 2b. The spectra were taken in a line across a hole with suspended $MoSe_2$. The extracted peak position, FWHM and amplitude are also shown. It is apparent that both the line position and the quality of the flake, as measured by PL intensity and linewidth, vary substantially across the flake. The quality is much higher in the middle (where the annealing laser was centered) than at the edges. The line position varies parabolically about the center, possibly due to some combination of larger strain gradient and more contaminants near the edges of the suspended area.

PL after raster scanning the annealing beam over the entire suspended area is shown in Fig. 2c. The spectra were taken across the same as above. In this case, the line position is almost constant over most of the sus-

pended area, changing by less than 1 meV (less than half the linewidth) over 6 µm. The PL intensity is also much more uniform, with the spatial FWHM being about 4 µm, as opposed to 2.5 µm before. The length scale of the spatial homogeneity in this case appears to be limited by the size of the hole. This is in stark contrast to exfoliated supported flakes, where the line center can shift by more than 10 meV over only a few microns. Even very high quality encapsulated samples can show linewidth-scale variation over < 3 µm [16], and 10 meV variation over ~ 15 µm [15]. We note that raster annealing with position-dependent annealing power could further improve homogeneity near the edges of the suspended. For the constant-power anneal performed here, the annealing temperature is higher when the beam is near the center because the center is more thermally isolated from the substrate.

When raster scanning the annealing beam, it is important that the final annealing position of the beam be at or near the center of the hole. This is likely due to strain effects. When the sample is cold, we hypothesize that the flake is essentially pinned on the substrate. However, when supported areas of the flake (especially those near the edge of the hole) are heated during the annealing, the flake can more readily slide across the substrate, changing the strain distribution. When annealing in the center, the areas of the flake at the edge of the hole are equally mobile. This ensures that the strain gradient in the suspended flake is minimized. If the final anneal spot is not centered, the flake could be more mobile on one side of the hole than on another, creating a non-uniform tensile force pulling from the edge of the hole. This would result in a strain gradient in the suspended monolayer. This strain gradient effect based upon the location of the final anneal spot is very repeatable — that is, after a full raster anneal one can alternately anneal near the edge of the sample and then in the middle, and the line position homogeneity changes accordingly. See Fig. S3 from the SI [30] for related plots of the PL homogeneity when the final anneal spot is not in the center, and for the repeatability of this effect.

IV. REPEATABILITY OF LASER ANNEALING

Annealing significantly improved sample quality on every spot investigated (> 40). However, there was variability in line position, linewidth and peak reflection/PL intensity. Fig. 3 shows reflection spectra both before and after annealing at 12 spots, as well as PL before and after for 12 different spots. Note that the holes were not pre- or post-selected in any way, other than to choose holes that did in fact have monolayer suspended $MoSe_2$. The data collected at each hole was post-selected in that each hole was annealed with successively higher laser power and the qualitatively best spectrum from each hole was selected. There is some variation in the optimal annealing power from hole to hole, which is discussed further below.

Reflection shows a marked change; in some cases the peak reflection increases by as much as 5× and in all cases improves significantly. Before annealing, there is a quite large reflectance from the suspended film, in some cases above 5%. For such a broadband reflection, this is much larger than one would expect from $MoSe_2$ alone [31]. We attribute this to a relatively thick layer of hydrocarbon contaminants on the suspended flake. The much lower broadband reflection after annealing indicates the removal of this layer. X-ray-photoelectron spectroscopy (XPS) measurements indicate that there is a hydrocarbon layer as thick as 5 nm on the $MoSe_2$. See Appendix A 9 for more details on the XPS measurements.

In PL, we see that both the X^- and X^D emission are reduced to below the noise floor for all 12 spots. The PL peak intensity increases for almost all spots, and the linewidth decreases by a factor of two for most spots. There is also a consistent blue shift of 10-15 meV after annealing. This is most likely due to a reduction in tensile strain [8], but could also be related to removing certain contaminants and dopants from the surface, possibly changing the effective dielectric environment seen by the exciton.

Samples exfoliated from bulk were also annealed, and behaved similarly to the CVD samples presented here. See Fig. S6 from the SI [30] for more details.

V. POWER DEPENDENCE OF LASER ANNEALING

The evolution of the annealed PL and reflection is shown as a function of annealing power in Figs. 4a and 4b. The X^- and X^D emission disappear at relatively low powers, and the red shift of the exciton primarily occurs at comparable or even lower powers. However, the PL linewidth and peak intensity improve to their best values only at significantly higher powers. The reflection linewidth and peak follow similar trends. The fact that the trion and defect emission are suppressed at relatively low annealing powers could indicate that the doping and defect emission are due to a species of adsorbate that binds less tightly to the layer. From the XPS measurements there appears to be a many-atom/molecule thick layer of contaminant on the flake before annealing. It is possible that the contaminants directly adsorbed to the $MoSe_2$ have larger activation energies of removal than those that are farther away and not directly adsorbed to the $MoSe_2$. A different explanation could be that the linewidth and peak intensity only improve at higher powers simply because they are more sensitive to small amounts of contaminants.

One last possible explanation is that desorption occurs primarily at lower powers and is responsible for the reduction of trion and defect emission, while strain reduction occurs primarily at higher powers and is responsible for the reduction in linewidth and increase in peak inten-

sity. However, additional work including studies monitoring the amount and type of contaminant present on the $MoSe_2$ as the annealing power is increased is needed to discern between these possibilities. This could be accomplished via a custom XPS, atomic force microscopy, or other measurement incorporated with a laser annealing setup.

As the annealing power is increased in Fig. 4b the linewidth of the reflection narrows somewhat, indicating a spectral concentration of oscillator strength due to reduction of inhomogeneous broadening. On the other hand, the peak reflectance increases much more quickly than the linewidth narrows. This indicates an overall increase in oscillator strength of the exciton during the annealing. As the material becomes more pristine, the coherence length of the exitonic wavefunction increases and it steals more and more oscillator strength from the band-to-band absorption. Note that while in principle the reduction in doping should transfer oscillator strength from the trion to the exciton, in practice this transfer was negligible because the samples used here had very low trion oscillator strength even before annealing.

When annealing with a nominally 700 nm diameter spot, the optimal annealing power (as measured by the power at which the PL/reflection linewidths are narrowest) varied from 400 µW to 800 µW for the CVD grown samples. Some, but not all, of this variation is likely due to small changes in the focusing conditions between different anneals. As the power was increased, some suspended flakes eventually began to degrade in quality. Others would snap and break before showing any signs of degradation. The PL in Fig. 4a is an example of a film that snapped before degrading, while the reflection in Fig. 4b is an example of a film that degraded before snapping. We posit that the main mode of failure is tearing of the flake due to tensile forces — those flakes with a higher concentration of defects as well as those under more tensile stress from their boundary conditions would break at lower temperatures and lower annealing powers.

The annealing temperature of the suspended $MoSe_2$ measured using Raman thermometry [32] is shown in 4c. The maximum temperature for this anneal was about 550 K, and as expected, the temperature varies linearly with excitation power. The PL intensity almost linearly tracks the excitation power.

For comparison, the PL and differential reflection after different-strength anneals and the associated annealing temperatures are shown for a supported flake in Figs. 4d and 4e. For the same annealing power, the supported flake does not reach as high temperature during annealing as the suspended flake because of heat conduction into the substrate. The PL of the supported $MoSe_2$ is very broad, with several features that are difficult to definitively assign labels. While the peak near 740 nm is likely X^0 emission, there is no clear X^- trion emission, and a broad emission X^D (likely associated with defects) extends several tens of nm to the red of X^0. As the annealing power is increased, the X^0 emission quickly decreases and the broad X^D emission decreases as well, but more slowly. At least based on the metric of PL and reflection, the annealing procedure seems to reduce the quality of supported samples.

It is unfortunate that the annealing process does not improve sample quality for the supported substrates used here, especially since so many applications of TMDCs employ supported substrates. One problem with annealing supported flakes is so-called photo-doping of the substrate, which can effectively charge dope the TMDC. Photo-doping is well-known to occur in SiO_2 [33] (which these samples are directly supported by) and involves photo-excitation of defect or impurity states. After the mobile electrons have migrated away, positive charges left behind in the substrate lead to long-lived charge accumulation and contribute to doping of the TMDC [34]. The rapid reduction of X^0 emission as annealing power increases in 4d is consistent with the photodoping hypothesis. One would expect to see an initial increase in X^- emission, which we do not here, followed by a possible decrease in overall PL [10] at very high doping levels, which is consistent with our results. While it is possible that the expected initial increase in X^- is masked by the defect emission, it seems more likely that there are additional factors preventing annealing from improving sample quality for supported flakes.

One obvious question to ask is whether contaminants trapped between the substrate and the $MoSe_2$ are more difficult to remove by heating. We hypothesize that heating should make contaminants more mobile in such a way that they will slowly diffuse out of the laser spot and become trapped in the colder regions at the edges of the laser spot. In this case, annealing should still improve sample quality, but a larger diameter beam and longer annealing times may be necessary. However, more work is needed on the subject to definitively tell whether or not this is the case. Specifically, studies investigating the annealing of supported $MoSe_2$ on highly crystalline substrates with low defect densities (to mitigate photodoping) and thermally annealing under high vacuum would be illuminating. Another strategy to mitigate substrate doping could be to use a properly-biased electrically-gated TMDC. Micro-scale roughness may also pin strain in supported structures in a way which is absent in suspended flakes. While heating the flake should make it more mobile, the heating may not be enough to entirely relax this strain. Further studies involving strain mapping before, after, and ideally during annealing using techniques such as those in [35] would help to answer these questions.

VI. TEMPORAL CHARACTERISTICS OF LASER ANNEALING

The PL and reflection as a function of annealing time are shown in Fig. 5. The annealing power is kept fixed, and the sample is annealed with 1 µs pulses. Since the

in-plane speed of sound in monolayer $MoSe_2$ should be similar to the ~ 600 m/s speed of MoS_2 [36], the time to reach thermal equilibrium for a hole with radius $\sim 4\,\mu$m is on the order of 7 ns, which is much shorter than the pulse length. This is experimentally supported by the observation that after fully annealing using many pulses, annealing using a CW beam of the same power does not change the PL/reflection of the sample. We can see that the PL improves quite quickly over the first ms, and afterwards changes much more slowly. The blue shift and reduction in broad defect PL both happen even more quickly, in about 10 and 50 µs, respectively. This is complementary to the fact that the blue shift of the exciton and trion/defect emission suppression occur at low powers in Fig. 4a. On the other hand, the reflection continues to improve even after 10 ms of annealing. This indicates that the peak reflectance is more sensitive and thus a better metric of sample quality than PL. This is supported by [16, 17], in which the peak reflectance is shown to be a measure of the ratio of radiative to non-radiative broadening.

VII. CONCLUSIONS AND OUTLOOK

The results presented here strongly indicate that the intrinsic quality of CVD-grown $MoSe_2$, and by extension other TMDCs including MoS_2, WS_2, and WSe_2 is comparably high to that of their mechanically-exfoliated-from-bulk counterparts. It seems necessary to completely remove contaminants that come from the growth and transfer processes, as well as from the ambient atmosphere. We have shown here that sample quality can be repeatably and dramatically increased, in some cases reaching PL linewidths and peak reflectances close to those of the highest quality encapsulated samples. The homogeneity of the samples appears to be limited by the size of the suspended area, offering a path forward for larger-area homogeneity than yet achieved in exfoliated samples.

We believe that this annealing procedure will enable further studies of exciton-polaritons, cavity QED with excitons, fundamental exciton physics and other many-body physics in TMDCs by providing a repeatable path to high-quality spatially-homogeneous TMDCs (and possibly all 2D materials). This annealing procedure will greatly aid efforts to create high quality arrays of quantum dots for quantum information processing, as well as networks of optical cavities coupled to TMDCs. The repeatability of the annealing as well as the large area and flexibility afforded by CVD-grown samples provides an avenue for scaling to multiple devices. Finally, the annealing procedure may also prove useful for electronic applications through an improvement in carrier mobility.

ACKNOWLEDGMENTS

This work was funded in part by the National Science Foundation (NSF) award PHY-1648807, by the NSF award DMR-1838497, and also by a seed grant from the Precourt Institute for Energy at Stanford University. Part of this work was performed at the Stanford Nano Shared Facilities (SNSF), supported by the NSF under award ECCS-1542152. CR, DG, and NB were supported in part by Stanford Graduate Fellowships. CR was also supported in part by a Natural Sciences and Engineering Research Council of Canada doctoral postgraduate scholarship. CR thanks Charles Hitzman for help performing and interpreting the XPS data. CR also thanks Ozgur Burak Aslan for discussions of strain effects in TMDC materials.

VIII. AUTHOR CONTRIBUTIONS

CR first noted the annealing effect, conceived the experiments, performed the experiments and performed the data analysis. HM suggested raster scanning the anneal, and annealing with a large diameter beam. CR and DG built the reflection/PL/Raman microscope setup, as well as the custom spectrometers. DG built the frequency doubling setup. CR and NB automated the measurements. All authors contributed to the manuscript.

Appendix A: Experimental Methods

1. Sample Preparation

The suspended CVD samples were purchased from 2DLayer. Their process involves growing monolayer $MoSe_2$ by CVD, and then transferring to 280 nm SiO_2 on Si substrates with patterned holes. While their process is proprietary, it is similar to the methods described in [22, 37]. The holes were approximately 20 µm deep and nominally 8 µm in diameter. The data in all figures except Fig. S6 from the SI [30] was taken using these samples.

A suspended sample was also prepared by starting with bulk $MoSe_2$ from 2D Semiconductor. The flake was exfoliated on to polydimethylsiloxane (PDMS) [38], and then directly transferred on to a holey silicon nitride grid from SPI Supplies (2 micron diameter holes in a 50 nm thick silicon nitride membrane). Data from this sample is shown in Fig. S6 from the SI [30].

2. Experimental Setup

All PL and reflection measurements were performed in a Montana Instruments Cryostation at a nominal base temperature of 4 K. The pressure was typically between

$1 \cdot 10^{-7}$ and $2 \cdot 10^{-7}$ Torr. The cryostat is equipped with an XYZ piezo stage stack from Attocube, on top of which the samples are mounted. A custom microscope assembly looks into the cryostat using a 20× Mitutoyo long-working-distance near-infra-red (NIR) objective with 0.7 mm of glass correction and a numerical aperture (NA) of 0.4. A removable beamsplitter couples light to a wide-field imaging path. See Fig. S9 from the SI [30]. There is a 0.5 mm thick glass window on the cryostat, and a 0.2 mm thick glass inner window on the cryostat heat shield, both of which are anti-reflection coated. An XY galvanometer pair is mounted directly behind the objective, which allows scanning of the spot over about 50 µm×50 µm. The entire microscope is also mounted on motorized XY translation stages which allow for translation of several mm, as well as a manual Z-stage which is used for focusing the microscope on the sample. Measurements were automated using the python instrument control package Instrumental, available on Github at https://github.com/mabuchilab/Instrumental.

3. PL Measurements

PL was measured by exciting using narrow linewidth ($< 1\,\mathrm{cm}^{-1}$ FWHM) 532 nm continuous wave (CW) beam obtained by frequency doubling a 1064 nm pump laser in periodically polled $LiNbO_3$ (PPLN). For the pump, a 10 mW 1064 nm seed from an NKT Koheras Adjustik laser was amplified using a Nufern nuamp amplifier. The 532 nm excitation laser was coupled onto the microscope by a single mode optical fiber and a reflective collimator. It is then coupled into the light path using a volume Bragg grating, which essentially functioned as a dichroic mirror (reflecting 532 nm while transmitting other wavelengths). This separates the PL from the excitation. Again, see Fig. S9 from the SI [30]. The excitation is then coupled into another single mode fiber, and the spectrum is measured using a home-built spectrometer. The spectrometer has an 1800 line/mm grating on a computer-controlled rotation stage, and spectra are measured on a Princeton Instruments PIXIS 2048 camera. The nominal resolution of the spectrometer is about $1\,\mathrm{cm}^{-1}$. The excitation power is measured before each spectrum by a power meter on a computer-controlled flip mount in the microscope setup. Typical excitation powers were about 3 µW at the sample. We did not observe significant changes in line shape when measuring at lower excitation powers.

4. Annealing

The annealing procedure was performed using the same 532 nm laser used for PL, except at much higher powers. The annealing was effective over a large range of spot sizes (we tested from 700 nm to 10 µm). As expected, the larger spots required correspondingly more laser power for optimal annealing. We typically annealed using a 700 nm spot for several seconds, although from Fig. 5 it can be seen that the annealing itself occurs in the first few ms. For a beam size of 700 nm the optimal annealing power the optimal annealing power was typically between 400 µW to 800 µW.

5. Reflection Measurements

Reflection was measured using a Thorlabs SLS201 broadband stabilized light source. Again, the incident beam was coupled on to the microscope through a single mode fiber. The power at the sample in the range of 700-800 nm was about 5 nW. The reflected beam was separated from the incident beam by a non-polarizing beamsplitter, and was coupled into a single mode fiber. Again, see Fig. S9 from the SI [30]. The spectrum was measured using the same spectrometer as for PL. Each reflection spectrum was calibrated by referencing it to the reflection of the bare substrate. The absolute reflection of the bare substrate was measured by in turn referencing to a silver mirror.

6. Reflection Analysis

When measuring reflection spectra from near the center of a suspended monolayer, the small back reflection (between 1% and 3% in most cases) from the bottom of the hole caused etalon interference fringes to appear in the measured spectrum. Even though the reflection was small, the etalon interference fringes were much larger, up to 10%. These fringes make the raw spectra difficult to interpret. Note that this was not an issue for the sample suspended on silicon nitride, since the holes in this case were through holes.

We fit the reflection spectra to a multilayer Fresnel model, which included a reflection from the bottom of the hole to account for the etalon. The dielectric constant of the film was the sum of a real background permittivity and an inhomogenous broadened Lorentzian oscillator to account for interaction with the exciton. Reflection from the trion is ignored, since it is assumed to contribute negligibly to the reflection. This is accurate for all but the highest carrier doping levels [10]. The background permittivity is meant to account for both the background permittivity of the $MoSe_2$ and any (possibly thick) layer of contaminants. The dielectric permittivity for a Lorentzian oscillator is:

$$\epsilon_r = \left[1 + \frac{\omega_p^2}{(\omega_0 - \omega^2) + i\gamma\omega}\right] \tag{A1}$$

where ϵ_r is the relative permittivity, ω is the optical frequency, ω_0 is the center frequency, γ represents homogenous broadening, and ω_p is related to the strength of the oscillator. The permittivity of the exciton is obtained by

convolving this Lorentzian with a Gaussian to account for inhomogeneous broadening.

The etalon length (hole depth), etalon reflection, oscillator center frequency, oscillator strength, oscillator homogenous broadening width, oscillator inhomogeneous broadening width, and film background permittivity were all fitted parameters. Once this model was fit to the raw data, the reflection from the suspended film alone could be extracted from the fitting parameters. Examples of the fits to raw data along with the raw data and extracted spectra are shown in Fig. S10 from the SI [30]. The raw spectra for each of the figures in the main text that shows fitted reflection data is also shown in the SI [30].

For the reflection measurements on a supported substrate, we use differential reflection $\frac{\Delta R}{R} = \frac{R_f - R}{R}$ where R_f is the reflection from the flake, and R is reflection from the bare substrate. The sigmoidal shape near the exciton resonance is consistent with other observations [3, 16], and the exact shape depends on interference conditions dictated by the thickness of the SiO_2 layer.

7. Thermal Model

The peak temperature during annealing is modeled using a steady-state radial heat equation with the absorption of the laser in the $MoSe_2$ treated as a point heat source. The annealing temperature is calculated as the temperature at one beam radius away from the point source. In the suspended case we set the temperature boundary condition at the edge of the hole to be the nominal base temperature of the cryostat, 4 K. With $u(r)$ as the radial temperature distribution, $q(r)$ as the heat flux density and k the thermal conductivity, the steady state heat equation is:

$$-k\nabla^2 u(r) = q(r) \tag{A2}$$

In the suspended 2D case with the boundary conditions above, the temperature distribution is:

$$u(r) = \frac{T_1 - T_0}{\ln\left(\frac{r_1}{r_0}\right)} \ln\left(\frac{r}{r_0}\right) + T_0 \tag{A3}$$

where T_1 is the temperature at radius r_1 (the beam radius), and T_0 is the temperature at r_0 (the edge of the hole). For a given input heat flux Q, the annealing temperature is then:

$$T_1 = \frac{Q \ln\left(\frac{r_0}{r_1}\right)}{2\pi k t_{\text{flake}}} + T_0 \tag{A4}$$

where t_{flake} is the thickness of the $MoSe_2$. The heat flux Q is the fraction of the incident laser power that is absorbed in the flake. We use a nominal value of 10% absorption in the flake at the laser wavelength of 532 nm, which is consistent with both [31] and our own measurements. The reduction in absorbed power due to PL re-emission is ignored since the PL quantum efficiency is small compared to unity. The quantum efficiency is in general small in TMDCs [1] and is even smaller at high powers [39] (which is the relevant power range for annealing). We use a thermal conductivity of 40 W/m·K for the $MoSe_2$, which is consistent with both theory and experiment [40, 41].

The supported case follows a similar analysis, except in this case we use infinite boundary conditions (the temperature goes to 4 K at large radius), and we assume that the thermal conductivity of the substrate dominates that of the flake. In this case, the annealing temperature is:

$$T_1 = \frac{Q}{2\pi k r_1} + T_0 \tag{A5}$$

We use a thermal conductivity of 2 W/m·K for the substrate, which is intermediate between that of SiO_2 and Si (but closer to that of SiO_2) in the relevant temperature range [42, 43]. The laser spot diameter was $r_1 = 350$ nm, and the hole radius was $r_0 = 4$ µm. Note that both models above ignore any temperature dependence of the thermal conductivity.

8. Raman Thermometry

Raman measurements were performed using the same 532 nm laser and the same beam path as for the PL measurements, except that an extra volume Bragg grating was used on the microscope to further knock out the excitation laser. This was necessary to prevent fiber Raman from overwhelming the Raman scattering from the $MoSe_2$, since the microscope was coupled to the spectrometer using a single mode fiber. A different home-built spectrometer was used for Raman measurements. This spectrometer has a 1200 line/mm blazed grating, and spectra are measured using a PIXIS 256 camera. The nominal resolution is about 1.5 cm^{-1}. There are two more volume Bragg gratings within the spectrometer, to further knock out the 532 nm excitation.

We used the $MoSe_2$ Raman peak at 242 cm^{-1} to perform Raman thermometry during the annealing process. Since the annealing process was in most cases at relatively low laser powers, the scattering signal was very weak and typical spectra would involve up to 10 exposures of 20 minutes each. The ratio between Stokes and anti-Stokes scattering is:

$$R = \frac{I_{\text{Stokes}}}{I_{\text{Anti-Stokes}}} = \left[\frac{\nu_0 - \Delta\nu}{\nu_0 + \Delta\nu}\right]^4 \exp\left[\frac{h\Delta\nu}{k_B T}\right] \tag{A6}$$

where I_{Stokes} and $I_{\text{Anti-Stokes}}$ are respectively the Stokes and anti-Stokes intensities, ν_0 is the laser frequency, $\Delta\nu$ is the Raman transition frequency, T is the temperature,

h is Planck's constant and k_B is the Boltzmann constant. The temperature is then:

$$T = \frac{h\Delta\nu}{k_B \ln\left[R\left[\frac{\nu_0+\Delta\nu}{\nu_0-\Delta\nu}\right]^4\right]} \tag{A7}$$

Some examples of the Raman spectra used in calculating the annealing temperature are shown in Fig. S11 from the SI [30].

9. XPS

We took XPS data from a supported area, assuming that the contaminants are qualitatively similar on suspended and supported areas. Data was taken on a PHI Versaprobe 3, on a monolayer of $\sim 100\,\mu$m dimensions using a $100\,\mu$m X-ray spot. This instrument uses 1486 eV X-rays and is sensitive to the top $\sim 10\,$nm of the sample. We used the machine calibration to extract atomic abundances using MultiPak software. A bulk sample of $MoSe_2$ from HQ Graphene was used as a further calibration for the relative abundance of Mo and Se. The raw XPS data for a supported flake is shown in Fig. S5a from the SI [30].

[1] Kin Fai Mak, Changgu Lee, James Hone, Jie Shan, and Tony F. Heinz, "Atomically thin mos_2: A new direct-gap semiconductor," Phys. Rev. Lett. **105**, 136805 (2010).

[2] Andrea Splendiani, Liang Sun, Yuanbo Zhang, Tianshu Li, Jonghwan Kim, Chi-Yung Chim, Giulia Galli, and Feng Wang, "Emerging photoluminescence in monolayer mos2," Nano Letters **10**, 1271–1275 (2010).

[3] Aaron M. Jones, Hongyi Yu, Nirmal J. Ghimire, Sanfeng Wu, Grant Aivazian, Jason S. Ross, Bo Zhao, Jiaqiang Yan, David G. Mandrus, Di Xiao, Wang Yao, and Xiaodong Xu, "Optical generation of excitonic valley coherence in monolayer wse2," Nature Nanotechnology **8**, 634 EP – (2013).

[4] Di Xiao, Gui-Bin Liu, Wanxiang Feng, Xiaodong Xu, and Wang Yao, "Coupled spin and valley physics in monolayers of mos_2 and other group-vi dichalcogenides," Phys. Rev. Lett. **108**, 196802 (2012).

[5] Kin Fai Mak, Keliang He, Jie Shan, and Tony F. Heinz, "Control of valley polarization in monolayer mos2 by optical helicity," Nature Nanotechnology **7**, 494 EP – (2012).

[6] Nardeep Kumar, Sina Najmaei, Qiannan Cui, Frank Ceballos, Pulickel M. Ajayan, Jun Lou, and Hui Zhao, "Second harmonic microscopy of monolayer mos_2," Phys. Rev. B **87**, 161403 (2013).

[7] Daniel B. S. Soh, Christopher Rogers, Dodd J. Gray, Eric Chatterjee, and Hideo Mabuchi, "Optical nonlinearities of excitons in monolayer mos_2," Phys. Rev. B **97**, 165111 (2018).

[8] Hiram J. Conley, Bin Wang, Jed I. Ziegler, Richard F. Haglund, Sokrates T. Pantelides, and Kirill I. Bolotin, "Bandgap engineering of strained monolayer and bilayer mos2," Nano Letters **13**, 3626–3630 (2013).

[9] Yumeng You, Xiao-Xiao Zhang, Timothy C. Berkelbach, Mark S. Hybertsen, David R. Reichman, and Tony F. Heinz, "Observation of biexcitons in monolayer wse2," Nature Physics **11**, 477 EP – (2015).

[10] Meinrad Sidler, Patrick Back, Ovidiu Cotlet, Ajit Srivastava, Thomas Fink, Martin Kroner, Eugene Demler, and Atac Imamoglu, "Fermi polaron-polaritons in charge-tunable atomically thin semiconductors," Nature Physics **13**, 255 EP – (2016).

[11] Ke Wang, Kristiaan De Greve, Luis A. Jauregui, Andrey Sushko, Alexander High, You Zhou, Giovanni Scuri, Takashi Taniguchi, Kenji Watanabe, Mikhail D. Lukin, Hongkun Park, and Philip Kim, "Electrical control of charged carriers and excitons in atomically thin materials," Nature Nanotechnology **13**, 128–132 (2018).

[12] Carmen Palacios-Berraquero, Dhiren M. Kara, Alejandro R. P Montblanch, Matteo Barbone, Pawel Latawiec, Duhee Yoon, Anna K. Ott, Marko Loncar, Andrea C. Ferrari, and Mete Atatüre, "Large-scale quantum-emitter arrays in atomically thin semiconductors," Nature Communications **8**, 15093 EP – (2017), article.

[13] R. F. Frindt, "Optical absorption of a few unit-cell layers of mos_2," Phys. Rev. **140**, A536–A539 (1965).

[14] Kin Fai Mak, Keliang He, Changgu Lee, Gwan Hyoung Lee, James Hone, Tony F. Heinz, and Jie Shan, "Tightly bound trions in monolayer mos2," Nature Materials **12**, 207 EP – (2012).

[15] F. Cadiz, E. Courtade, C. Robert, G. Wang, Y. Shen, H. Cai, T. Taniguchi, K. Watanabe, H. Carrere, D. Lagarde, M. Manca, T. Amand, P. Renucci, S. Tongay, X. Marie, and B. Urbaszek, "Excitonic linewidth approaching the homogeneous limit in mos_2-based van der waals heterostructures," Phys. Rev. X **7**, 021026 (2017).

[16] Giovanni Scuri, You Zhou, Alexander A. High, Dominik S. Wild, Chi Shu, Kristiaan De Greve, Luis A. Jauregui, Takashi Taniguchi, Kenji Watanabe, Philip Kim, Mikhail D. Lukin, and Hongkun Park, "Large excitonic reflectivity of monolayer $mose_2$ encapsulated in hexagonal boron nitride," Phys. Rev. Lett. **120**, 037402 (2018).

[17] Patrick Back, Sina Zeytinoglu, Aroosa Ijaz, Martin Kroner, and Atac Imamoğlu, "Realization of an electrically tunable narrow-bandwidth atomically thin mirror using monolayer $mose_2$," Phys. Rev. Lett. **120**, 037401 (2018).

[18] Lukas Mennel, Marco M. Furchi, Stefan Wachter, Matthias Paur, Dmitry K. Polyushkin, and Thomas Mueller, "Optical imaging of strain in two-dimensional crystals," Nature Communications **9**, 516 (2018).

[19] Jinhua Hong, Zhixin Hu, Matt Probert, Kun Li, Danhui Lv, Xinan Yang, Lin Gu, Nannan Mao, Qingliang Feng, Liming Xie, Jin Zhang, Dianzhong Wu, Zhiyong Zhang, Chuanhong Jin, Wei Ji, Xixiang Zhang, Jun Yuan, and Ze Zhang, "Exploring atomic defects in molybdenum disulphide monolayers," Nature Communications **6**, 6293 EP – (2015), article.

[20] Haining Wang, Changjian Zhang, and Farhan Rana, "Ultrafast dynamics of defect-assisted electron-hole recombination in monolayer mos2," Nano Letters **15**, 339–345 (2015).

[21] Jiamin Xue, Javier Sanchez-Yamagishi, Danny Bulmash, Philippe Jacquod, Aparna Deshpande, K. Watanabe, T. Taniguchi, Pablo Jarillo-Herrero, and Brian J. LeRoy, "Scanning tunnelling microscopy and spectroscopy of ultra-flat graphene on hexagonal boron nitride," Nature Materials **10**, 282 EP – (2011).

[22] Yifei Yu, Chun Li, Yi Liu, Liqin Su, Yong Zhang, and Linyou Cao, "Controlled scalable synthesis of uniform, high-quality monolayer and few-layer mos2 films," Scientific Reports **3**, 1866 EP – (2013), article.

[23] YiHsien Lee, XinQuan Zhang, Wenjing Zhang, MuTung Chang, ChengTe Lin, KaiDi Chang, YaChu Yu, Jacob TseWei Wang, ChiaSeng Chang, LainJong Li, and TsungWu Lin, "Synthesis of largearea mos2 atomic layers with chemical vapor deposition," Advanced Materials **24**, 2320–2325.

[24] Haiyan Nan, Zilu Wang, Wenhui Wang, Zheng Liang, Yan Lu, Qian Chen, Daowei He, Pingheng Tan, Feng Miao, Xinran Wang, Jinlan Wang, and Zhenhua Ni, "Strong photoluminescence enhancement of mos2 through defect engineering and oxygen bonding," ACS Nano **8**, 5738–5745 (2014).

[25] Joshua D Wood, Gregory P Doidge, Enrique A Carrion, Justin C Koepke, Joshua A Kaitz, Isha Datye, Ashkan Behnam, Jayan Hewaparakrama, Basil Aruin, Yaofeng Chen, Hefei Dong, Richard T Haasch, Joseph W Lyding, and Eric Pop, "Annealing free, clean graphene transfer using alternative polymer scaffolds," Nanotechnology **26**, 055302 (2015).

[26] Matin Amani, Robert A. Burke, Xiang Ji, Peida Zhao, Der-Hsien Lien, Peyman Taheri, Geun Ho Ahn, Daisuke Kirya, Joel W. Ager, Eli Yablonovitch, Jing Kong, Madan Dubey, and Ali Javey, "High luminescence efficiency in mos2 grown by chemical vapor deposition," ACS Nano **10**, 6535–6541 (2016).

[27] Matthias Florian, Malte Hartmann, Alexander Steinhoff, Julian Klein, Alexander W. Holleitner, Jonathan J. Finley, Tim O. Wehling, Michael Kaniber, and Christopher Gies, "The dielectric impact of layer distances on exciton and trion binding energies in van der waals heterostructures," Nano Letters **18**, 2725–2732 (2018).

[28] C. Robert, D. Lagarde, F. Cadiz, G. Wang, B. Lassagne, T. Amand, A. Balocchi, P. Renucci, S. Tongay, B. Urbaszek, and X. Marie, "Exciton radiative lifetime in transition metal dichalcogenide monolayers," Phys. Rev. B **93**, 205423 (2016).

[29] Sefaattin Tongay, Jian Zhou, Can Ataca, Jonathan Liu, Jeong Seuk Kang, Tyler S. Matthews, Long You, Jingbo Li, Jeffrey C. Grossman, and Junqiao Wu, "Broad-range modulation of light emission in two-dimensional semiconductors by molecular physisorption gating," Nano Letters **13**, 2831–2836 (2013).

[30] See Supplemental Material at [URL will be inserted by publisher] for raw un-fitted reflection plots corresponding to the relevant plots in the main text, details of the XPS and Raman analysis, spectra from an exfoliated suspended flake, experimental setup shematics, and more details on raster annealing.

[31] Yilei Li, Alexey Chernikov, Xian Zhang, Albert Rigosi, Heather M. Hill, Arend M. van der Zande, Daniel A. Chenet, En-Min Shih, James Hone, and Tony F. Heinz, "Measurement of the optical dielectric function of monolayer transition-metal dichalcogenides: mos_2, $MoSe_2$, ws_2, and WSe_2," Phys. Rev. B **90**, 205422 (2014).

[32] R. Loudon, "The raman effect in crystals," Advances in Physics **13**, 423–482 (1964).

[33] Isidoro Martinez, Mário Ribeiro, Pablo Andres, Luis E. Hueso, Fèlix Casanova, and Farkhad G. Aliev, "Photodoping-driven crossover in the low-frequency noise of mos_2 transistors," Phys. Rev. Applied **7**, 034034 (2017).

[34] L. Ju, J. Velasco Jr, E. Huang, S. Kahn, C. Nosiglia, Hsin-Zon Tsai, W. Yang, T. Taniguchi, K. Watanabe, Y. Zhang, G. Zhang, M. Crommie, A. Zettl, and F. Wang, "Photoinduced doping in heterostructures of graphene and boron nitride," Nature Nanotechnology **9**, 348 EP – (2014).

[35] Yimo Han, Kayla Nguyen, Michael Cao, Paul Cueva, Saien Xie, Mark W. Tate, Prafull Purohit, Sol M. Gruner, Jiwoong Park, and David A. Muller, "Strain mapping of two-dimensional heterostructures with subpicometer precision," Nano Letters **18**, 3746–3751 (2018), pMID: 29775315, https://doi.org/10.1021/acs.nanolett.8b00952.

[36] Yongqing Cai, Jinghua Lan, Gang Zhang, and Yong-Wei Zhang, "Lattice vibrational modes and phonon thermal conductivity of monolayer mos_2," Phys. Rev. B **89**, 035438 (2014).

[37] Alper Gurarslan, Yifei Yu, Liqin Su, Yiling Yu, Francisco Suarez, Shanshan Yao, Yong Zhu, Mehmet Ozturk, Yong Zhang, and Linyou Cao, "Surface-energy-assisted perfect transfer of centimeter-scale monolayer and few-layer mos2 films onto arbitrary substrates," ACS Nano **8**, 11522–11528 (2014), pMID: 25347296, https://doi.org/10.1021/nn5057673.

[38] Andres Castellanos-Gomez, Michele Buscema, Rianda Molenaar, Vibhor Singh, Laurens Janssen, Herre S J van der Zant, and Gary A Steele, "Deterministic transfer of two-dimensional materials by all-dry viscoelastic stamping," 2D Materials **1**, 011002 (2014).

[39] Shinichiro Mouri, Yuhei Miyauchi, Minglin Toh, Weijie Zhao, Goki Eda, and Kazunari Matsuda, "Nonlinear photoluminescence in atomically thin layered wse_2 arising from diffusion-assisted exciton-exciton annihilation," Phys. Rev. B **90**, 155449 (2014).

[40] Yang Hong, Jingchao Zhang, and Xiao Cheng Zeng, "Thermal conductivity of monolayer mose2 and mos2," The Journal of Physical Chemistry C **120**, 26067–26075 (2016).

[41] Xian Zhang, Dezheng Sun, Yilei Li, Gwan-Hyoung Lee, Xu Cui, Daniel Chenet, Yumeng You, Tony F. Heinz, and James C. Hone, "Measurement of lateral and interfacial thermal conductivity of single- and bilayer mos2 and mose2 using refined optothermal raman technique," ACS Applied Materials & Interfaces **7**, 25923–25929 (2015).

[42] C. J. Glassbrenner and Glen A. Slack, "Thermal conductivity of silicon and germanium from 3°k to the melting point," Phys. Rev. **134**, A1058–A1069 (1964).

[43] Da-Jeng Yao, Wei-Chih Lai, and Heng-Chieh Chien, "Temperature dependence of thermal conductivity for silicon dioxide," 2008 Proceedings of the ASME Micro/Nanoscale Heat Transfer International Conference, MNHT 2008 , 435–439 (2008).

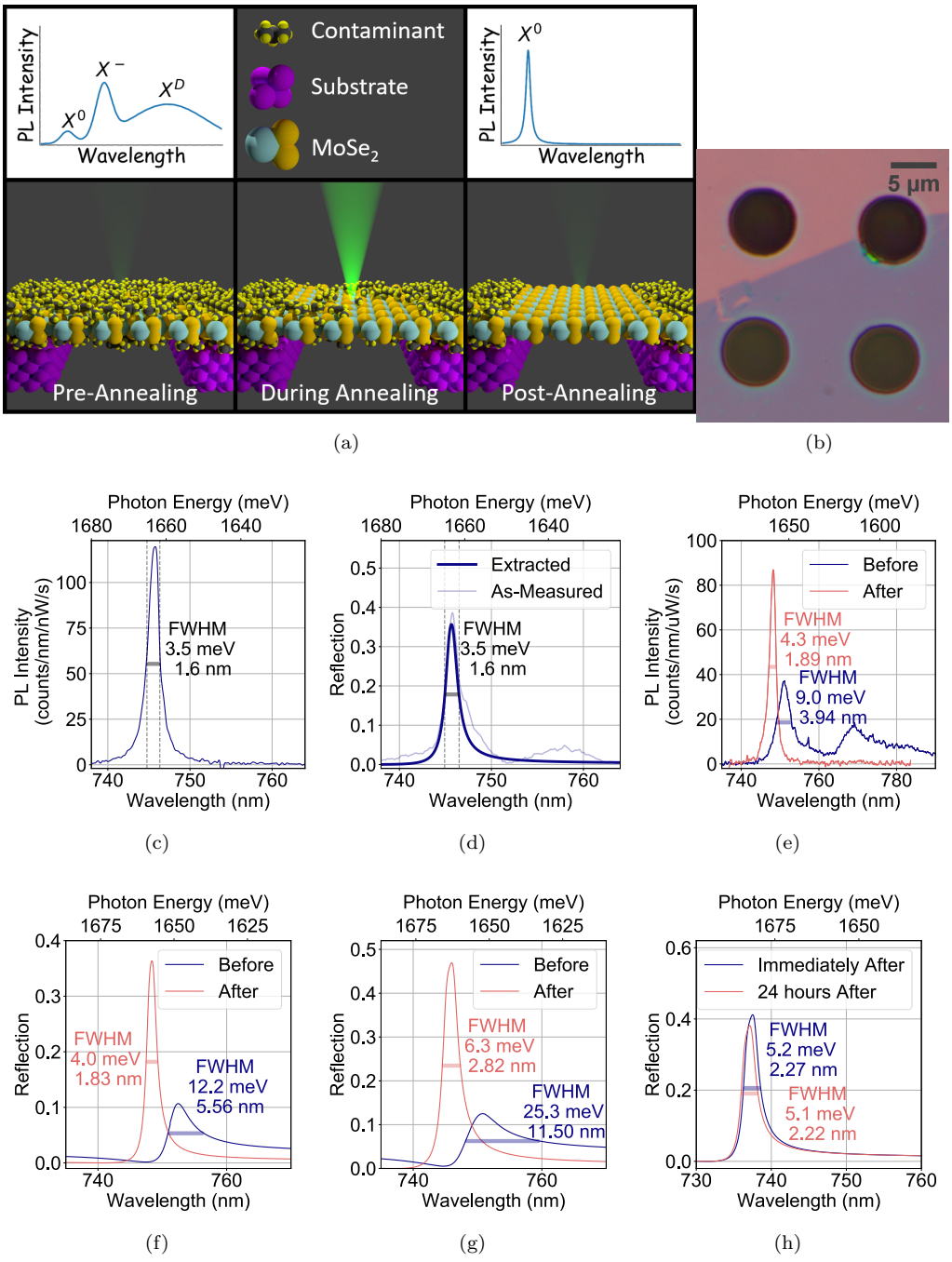

FIG. 1. Sample improvement from annealing. A schematic (a) of the annealing process showing a suspended flake before, during, and after annealing. Note that atoms sizes are not to scale with the laser spot and sample dimensions. The inset spectra illustrate typical PL before and after annealing. Neutral exciton emission is labelled X^0, negatively charged trion emission is labelled X^- and the broad peak typically associated with defect emission is labelled X^D. The optical microscope image (b) of a typical sample with four dark holes visible in the substrate, the lower two of which have suspended monolayer $MoSe_2$. The darker portion of the substrate has supported monolayer $MoSe_2$. PL (c) and reflection (d) from the same position of suspended monolayer CVD-grown $MoSe_2$ annealed for 1 minute with 9 mW laser power and a 10 µm spot size. Note that in (d) the reflection from the suspended film alone has been extracted from the raw reflection using a fitting procedure described in Appendix A 6 to remove interference fringes from reflections off the bottom of hole in the silicon substrate. PL (e) and reflection (f) from a second position of monolayer suspended CVD-grown $MoSe_2$ annealed for 5 minutes with 500 µW laser power with a 700 nm spot size. Reflection (g) before and after from a third position, which had the highest reflection after annealing. Reflection (h) immediately after annealing and 24 hours after annealing, from a fourth position. Measurement and annealing was at 4K, and $2 \cdot 10^{-7}$ Torr pressure. The corresponding unfitted reflection spectra for (f), (g) and (h) are shown in Fig. S1 from the SI [30].

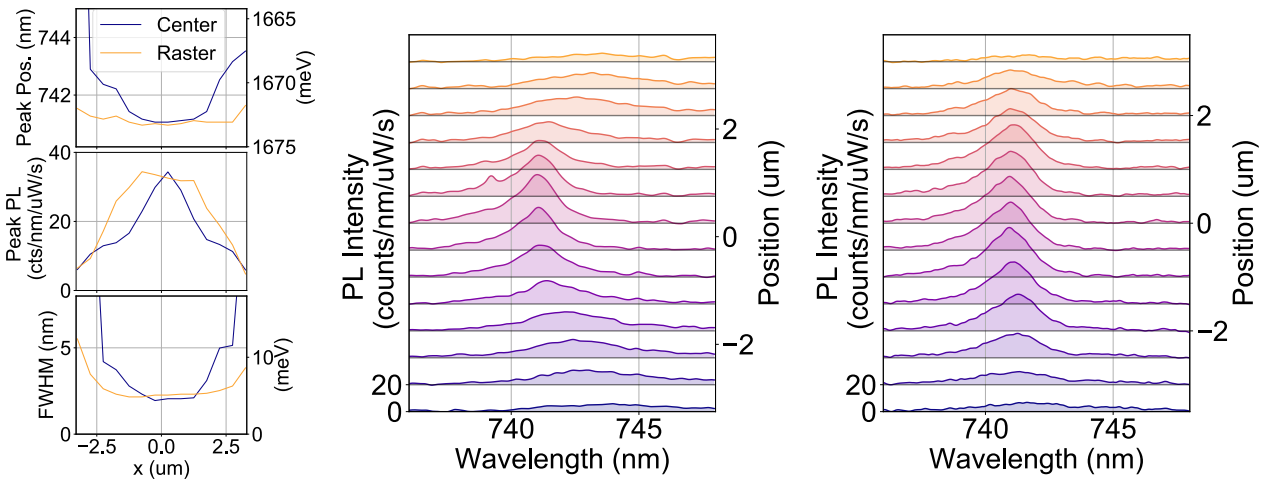

(a) (b) (c)

FIG. 2. PL homogeneity improvement from raster scanning the annealing laser. FWHM, peak amplitude and peak position (a) for the exciton PL from a line across a hole first annealed in the center, then annealed by raster scanning a spot over the entire hole. Each spot was annealed at 400 µW for 1 s with a 700 nm spot size. PL along the same line for an initial anneal at the center (b), and for a raster-scanned anneal (c).

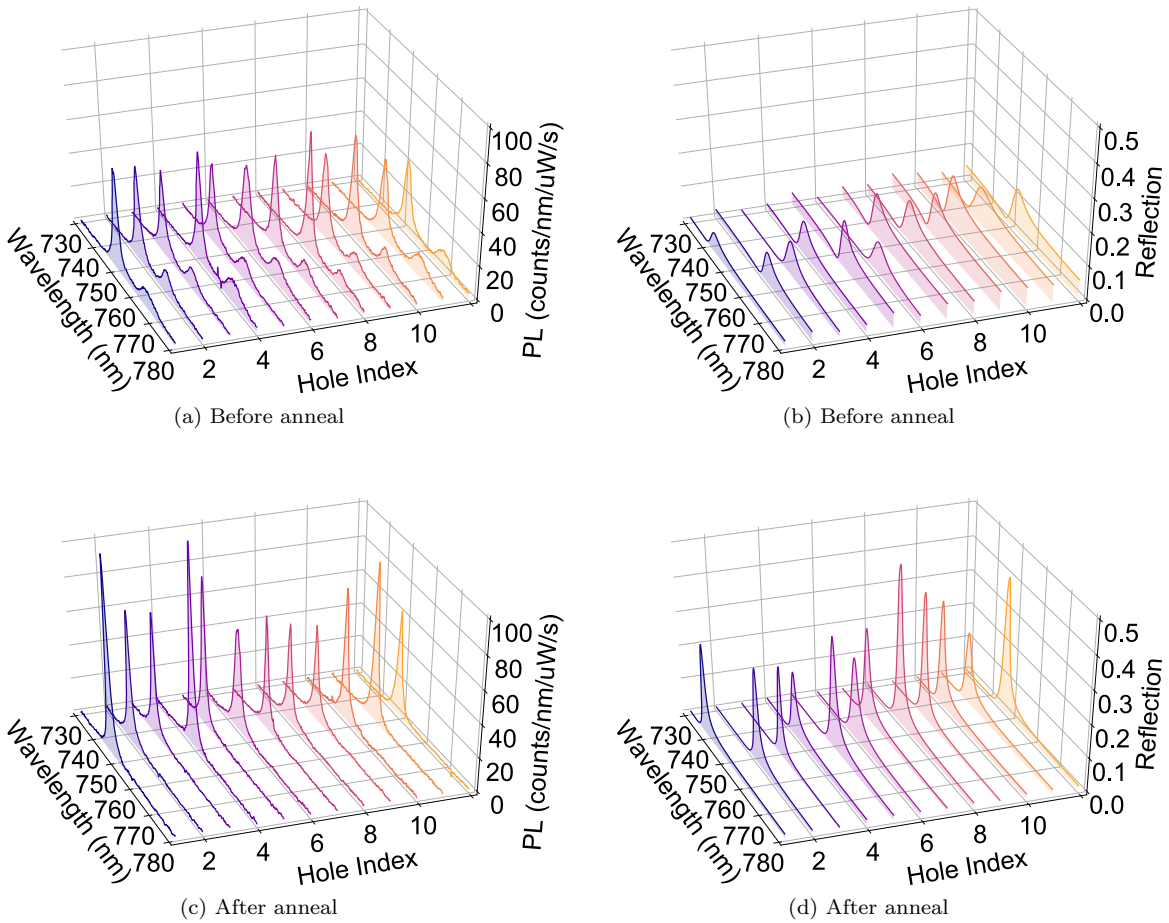

(a) Before anneal

(b) Before anneal

(c) After anneal

(d) After anneal

FIG. 3. Repeatability of the annealing process. PL and reflection before and after for 12 separate holes. The PL before annealing (a) and after annealing (c). The reflection before annealing (b) and after annealing (d). Note that the PL and reflection are from different sets of 12 holes. The holes were annealed in the center using a 700 nm diameter laser spot. Power was increased incrementally, and the best spectra was chosen. There was no pre- or post-selection of holes. The reflection spectra are fit as explained in Appendix A 6, and the corresponding raw spectra are shown in Fig. S4 from the SI [30].

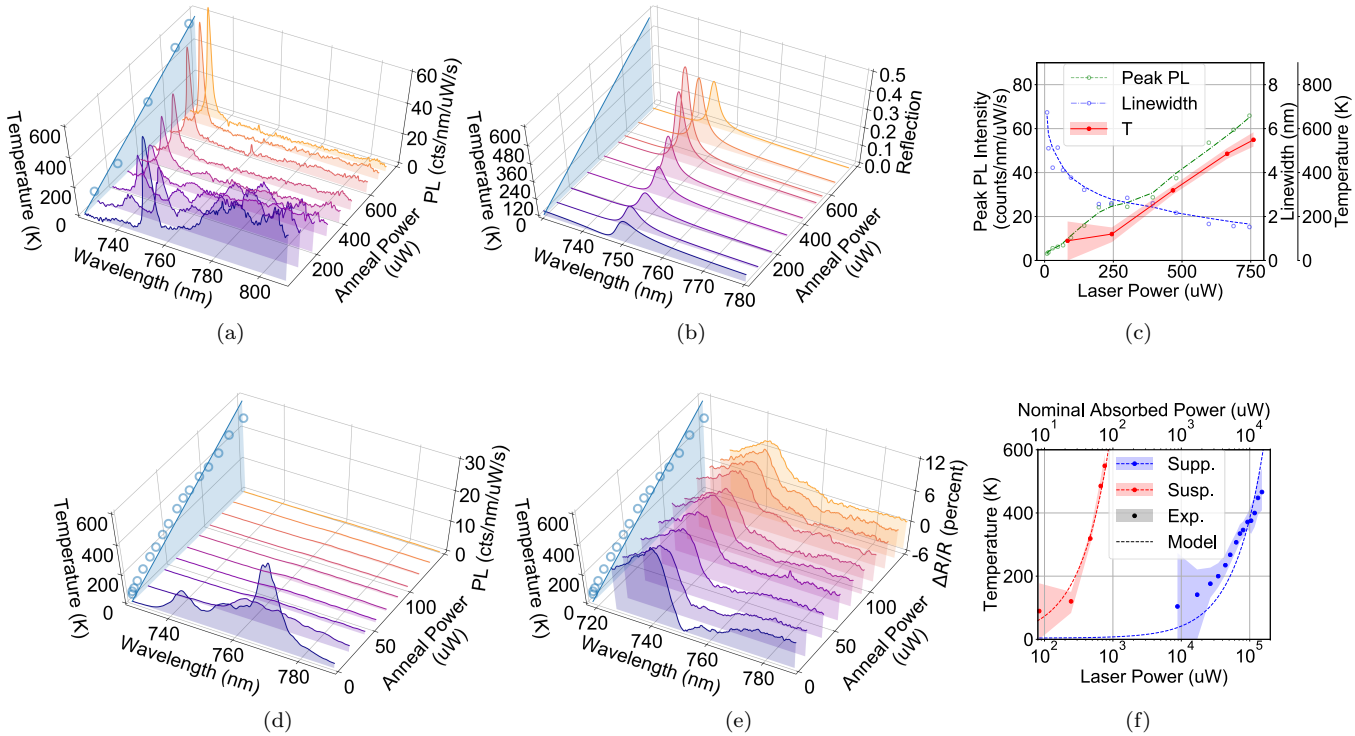

FIG. 4. Annealing power dependence of sample quality. The PL (a) and reflection (b) after annealing a suspended $MoSe_2$ monolayer for successively increasing laser annealing power. The modeled (line) and measured (circles) temperature are also shown in blue. Note that the PL and reflection are from different holes. Peak amplitude and width of the exciton PL (c), alongside the measured annealing temperature (T). The peak and width are extracted from the data in (a), and the lines shown are filtered versions of the data (circles) meant as a guide to the eye. PL (d) and (un-fitted) differential reflection (e) after annealing a supported monolayer on 280 nm SiO_2 on Si for successively increasing powers. Again, the modeled (line) and measured (circles) temperature are also shown in blue. Note that the PL and differential reflection are from nearby but slightly separated spots. Experimentally measured (Exp.) and modeled temperature during annealing (f) for both supported (Supp.) and suspended (Susp.) samples. The shaded area represents the uncertainty in the temperature measurement. The raw reflection spectra corresponding to the fitted reflection spectra are shown in S7 from the SI [30].

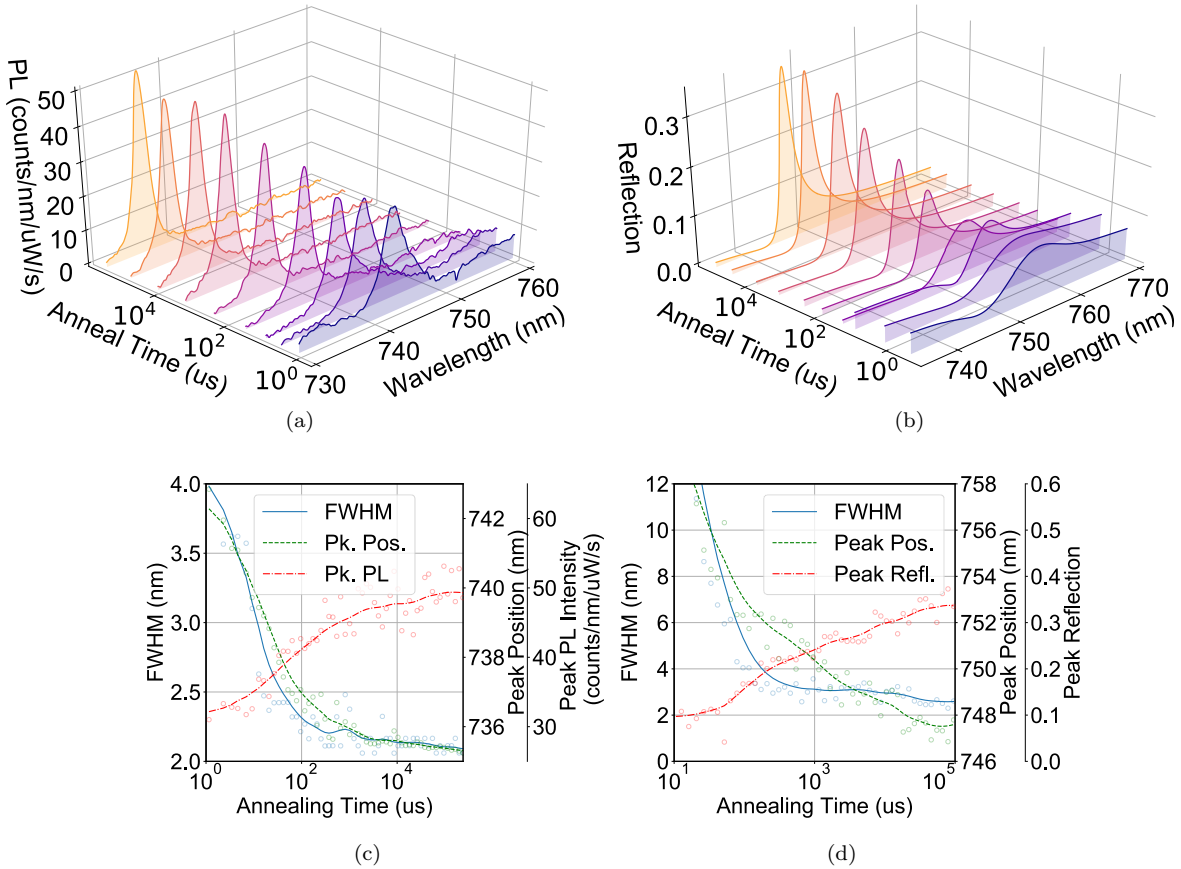

FIG. 5. Temporal evolution of the annealing process. Behavior as a function of total annealing time of the PL (a) and reflection (b) for a CVD-grown suspended $MoSe_2$ monolayer. The flake was annealed in 1 µs increments, with a laser power of 500 µW at 532 nm. Spectra were taken at selected intervals. The behavior of the extracted peak position, amplitude and FWHM for PL (c) and for reflection (d). The lines in (c) and (d) are filtered versions of the data, shown by the dots, and serve as a guide to the eye. Corresponding plots of the unfitted reflection spectras for (b) and (d) are shown in Fig. S8 from the SI [30].